Modelling of adsorption and intercalation of hydrogen on/into tungsten disulphide multilayers and multiwall nanotubes

José I. Martínez,[a,*] Alex Laikhtman,[b] Hoi Ri Moon,[c] Alla Zak,[b] and Julio A. Alonso[d,†]

Understanding the interaction of hydrogen with layered materials is crucial in the fields of sensors, catalysis, fuel cells and hydrogen storage, among others. Density functional theory, improved by the introduction of van der Waals dispersion forces, provides an efficient and practical workbench to investigate the interaction of molecular and atomic hydrogen with WS_2 multilayers and nanotubes. We find that H_2 physisorbs on the surface of those materials on top of W atoms, while atomic H chemisorbs on top of S atoms. In the case of nanotubes, the chemisorption strength is sensitive to the nanotube diameter. Diffusion of H_2 on the surface of WS_2 encounters quite small activation barriers whose magnitude helps to explain previous and new experimental results for the observed dependence of the hydrogen concentration with temperature. Intercalation of H_2 between adjacent planar WS_2 layers reveals an endothermic character. Intercalating H atoms is energetically favorable, but the intercalation energy does not compensate for the cost of dissociating the molecules. When H_2 molecules are intercalated between the walls of a double wall nanotube, the rigid confinement induces the dissociation of the confined molecules. A remarkable result is that the presence of a full H_2 monolayer adsorbed on top of the first WS_2 layer of a WS_2 multilayer system strongly facilitates the intercalation of H_2 between WS_2 layers underneath. This opens up an additional gate to intercalation processes.

1. Introduction

After graphene, a new generation of layered two-dimensional (2D) materials has emerged due to their excellent electronic, optical and mechanical properties. Within this family, hexagonal boron nitride (h-BN), some transition metal oxides, transition metal dichalcogenides (TMDCs), and new materials such as black phosphorus, germanene and antimonene, cover a wide range of properties expected to be profitable in diverse applications.[1] In particular, TMDCs are formed by chalcogen elements (X = S, Se, Te, among others) and transition metals (M = Mo, W, Ti, Zr, Hf, among others) piled up in a layered structure. Here the molecular MX_2 layers are bonded to each other by weak van der Waals forces, while each molecular layer consists of an atomic metal layer sandwiched by two atomic chalcogen layers (X-M-X) bonded by strong covalent bonds. The layers can be easily exfoliated, as it occurs with graphene layers in graphite.

Single MX_2 layers often show different properties compared to their corresponding bulk materials. For instance, these materials present electronic band-gaps whose magnitude depends on the number of stacked layers. Moreover, Mak *et al.*[2] and Splendiani *et al.*[3] demonstrated that monolayers of trigonal prismatic MoS_2 undergo an *indirect-to-direct* electronic band gap transition which originates from quantum confinement. As a result, strong photoluminescence emerges, so offering novel applications of such monolayers for a

variety of electronic and optical devices. Atomic defects in the layers can act locally as catalytic regions. All these properties make dichalcogenide nanostructures composed of one or a few-layers very appealing for applications in different fields: sensors and biosensors,[4] nanoelectronics,[4-6] optoelectronics,[5-7] spintronics,[1] catalysis,[1,7] energy storage,[8,9] and hydrogen storage.[10] Studies of transition metal chalcogenides (CoS, CuS)[11,12] and dichalcogenides (WS_2, VS_2)[13-15] have delivered promising results towards the development of optical and electrochemical sensors and biosensors.

The interaction of hydrogen with a variety of materials is highly relevant to the development of hydrogen cells and hydrogen storage. Novel storage methods have been proposed which are intended to replace the present technology of storing hydrogen in steel tanks at high pressures. One of these alternative techniques involves storing hydrogen in porous and layered materials. The storage mechanism in this case is based on the adsorption of molecular hydrogen on the inner surface of the pores, or in between adjacent layers. Thus, a large effective area available for adsorption is likely to result in a large amount of stored hydrogen. Storage in porous carbons and carbon nanotubes has been studied in depth, both experimentally[16] and by computer simulations.[17] The atomic structure of the pore walls in porous carbons is similar to that of graphene ribbons, although often curved and with abundant defects.[18] The interaction between H_2 and the graphitized walls is weak and dominated by dispersion interactions.

Functionalization of the surface of layered materials with atomic hydrogen can be used to change their properties. For instance, a variety of chemisorbed hydrogen dimer structures was formed upon room-temperature adsorption of atomic hydrogen on single layer graphene grown on SiC(0001).[19] In such a way a local doping of the graphene lattice was induced. Besides, it has been reported that the chemisorption of atomic H generates a magnetic moment in graphene. The magnetic moment is characterized by a ~20 meV

[a.] *Materials Science Factory, Institute of Materials Science of Madrid (ICMM-CSIC), 3 Sor Juana Inés de la Cruz St., 28049 Madrid (Spain)*

[b.] *Faculty of Sciences, Holon Institute of Technology (HIT), 52 Golomb St., Holon, 5810201 Holon (Israel)*

[c.] *Department of Chemistry, Ulsan National Institute of Science and Technology, 44919 Ulsan (Republic of Korea)*

[d.] *Departamento de Física Teórica, Atómica y Óptica, University of Valladolid, 47011 Valladolid (Spain)*

* E-mail: joseignacio.martinez@icmm.csic.es

† E-mail: jaalonso@fta.uva.es

spin-split state at the Fermi energy, essentially localized on the carbon sublattice opposite to the one where the hydrogen atom is chemisorbed.[20] Additionally, full functionalization of graphene with hydrogen produces a material, graphane, with different electronic properties.[21] In the case of TMDCs, the modification of the electronic properties of MoS_2 due to hydrogen adsorption is the basis for the construction of hydrogen chemical sensors with this material.[22]

The interaction between hydrogen and inorganic layered materials has been explored to a much lower extent than for carbon-based structures. The hydrogen storage properties of multiwall nanotubes of MoS_2, TiS_2, and BN were investigated in several studies.[23,24] Tenne and co-workers were the first who reported that the TMDCs with layered structures, like WS_2 and MoS_2, can form closed-cage nanoparticles with polyhedral or nanotubular shapes.[25] An experimental investigation of the interaction of hydrogen with WS_2 nanotubes and fullerenic-like nanoparticles, and the capacity of these materials to store hydrogen, has been reported in two previous publications,[10,26] and some preliminary ideas on the interaction have been proposed.[26,27] Various hydrogenation methods were applied in those experiments: hydrogenation by high-pressure molecular hydrogen, as well as microwave and radiofrequency (RF) plasma-enhanced hydrogenation performed at low gas pressures. Our main goal in this work is to further elucidate the details of the interaction between hydrogen and WS_2. For that purpose we present an exhaustive theoretical first-principles investigation of different aspects of the interaction between hydrogen and different varieties of layered WS_2 materials: single layers, multilayers and nanotubes. We have investigated adsorption of atomic and molecular hydrogen on the surfaces, dissociation of H_2, diffusion, and intercalation between the WS_2 layers, which can help to interpret the results of the hydrogenation experiments. In addition, we present some new experimental results on hydrogen adsorption that can be interpreted in the light of the diffusion calculations.

The theoretical methods used in the calculations are presented in Section 2, and the pure WS_2 materials, planar multilayers and nanotubes are described in Section 3. Sections 4 and 5 present the results of the adsorption of molecular and atomic hydrogen, respectively. The study of the diffusion of molecular and atomic hydrogen in Section 6 is used to interpret new hydrogenation experiments also reported in that Section. The intercalation of hydrogen between layers in multilayers and double-walled nanotubes is investigated in Section 7, and the Raman spectrum of physisorbed H_2 molecules is modelled in Section 8. The conclusions of this work are summarized in Section 9.

2. Computational Methods

Atomistic simulations for planar and curved layered WS_2 materials, clean and with hydrogen adsorbed, have been performed with the density functional formalism (DFT), as implemented in the plane-wave package QUANTUM ESPRESSO.[28] Only valence electrons have been explicitly taken into account, and the ionic cores have been described by Projector Augmented Wave (PAW)

pseudopotentials.[29] The Perdew-Burke-Ernzerhof (PBE) generalized gradient approximation (GGA) functional[30] has been used for electronic exchange and correlation (XC) effects. Because long-range dispersion interactions are expected to be relevant in the interaction between hydrogen and the WS_2 surface, a perturbative van der Waals correction was applied. For this purpose, we have used an empirical r^{-6} correction to add dispersive forces to conventional density functionals within the DFT+D formalism.[31-33] To optimize the geometrical configurations, structural relaxations were performed within a conjugate-gradient minimization scheme until the maximum force on any atom was below 0.01 eV Å^{-1}. The self-consistent calculations were performed with a plane-wave cut-off of 500 eV. The Fermi level was smeared out using the Methfessel-Paxton approach[34] with a Gaussian width of 0.01 eV, and all energies were extrapolated to T=0 K. The Brillouin zone was sampled by employing optimal Monkhorst-Pack grids.[35] With these setups, total energies are converged to a precision better than 10^{-6} eV, and adsorption energies are obtained with accuracies of 0.01 eV.

Apart from the enthalpies of H_2 adsorption and dissociation, an important feature to ascertain the competition between molecular adsorption and dissociative chemisorption is the height of the dissociation barrier. Transition states have been investigated herein with the climbing-image nudged elastic band (CI-NEB) approach[36-38] implemented in the QUANTUM ESPRESSO package,[28] where the initial, final, and a sufficient number of intermediate image-states (30 in the present case) were free to fully relax. This CI-NEB method has several advantages: i) it converges to a minimum energy path (MEP), providing sufficient resolution in the discrete representation of the path when enough images are included in the seeking process; ii) it only requires evaluation of the interaction energy and the first derivative of the energy with respect to coordinates; iii) the convergence to the MEP is decoupled from the discrete representation of the path, making the former robust and the latter flexible; iv) the method guarantees obtaining a continuous path even when multiple MEPs exist. Within this approach we have computed the minimum energy paths, as well as the height of the corresponding energy barriers at the transition states for surface diffusion of atomic and molecular hydrogen, and for dissociation of H_2 on the WS_2 surface.

We have used a supercell approach and periodic boundary conditions to model the layered WS_2 materials: a single planar layer, a trilayer, a surface, and the bulk crystal. In the calculations for the layer, trilayer and surface we have considered a distance of about 25 Å of empty space between neighbouring supercells along the direction perpendicular to the layers (say, the z-axis). To obtain the optimal structures, the positions of all the atoms were allowed to fully relax during the optimizations, and the lattice parameters along the two directions parallel to the layers were optimized. To model the WS_2 surface, five layers were considered, and the distance between the two bottom layers was kept fixed at the calculated bulk separation. The Brillouin zone for all the systems was sampled by using a [4×4×1] Monkhorst-Pack grid, guaranteeing good convergence in energy and electronic density. In the (4×4) unit cell of all the layered systems considered, the unit cell in each WS_2 layer, with optimized size of (12.6×12.6) Å^2, contains 48 atoms (16 W and 32 S atoms) showing perfectly balanced WS_2 stoichiometry.

We have also investigated a large variety of WS_2 nanotubes (NTs). Periodic boundary conditions have been applied along the longitudinal tube axis, to model nanotubes of infinite length. In addition, we have taken a distance of at least 15 Å between neighbouring supercells along the two lateral directions perpendicular to the nanotube axis. All the atom positions were allowed to fully relax in the structural optimization process, and the lattice parameter parallel to the nanotube axis was fully optimized. The Brillouin zone for all the nanotube systems was sampled by using a [8×1×1] Monkhorst-Pack grid, once again guaranteeing good convergence in energy and electronic density.

3. Planar and Curved Layered WS_2 Materials

Tungsten disulphide is a compound formed by WS_2 layers. Each layer is itself a sandwich formed by two planes of sulphur atoms with a plane of tungsten atoms in between. The chemical bonding between W and S atoms is strong inside each sandwich, where each W atom is coordinated to six S atoms forming a trigonal prism. On the other hand, the bonding between adjacent WS_2 layers is weak. The calculated inter-layer distance in the bulk (distance between the W planes) is 6.15 Å, which deviates by only 1.2 % from the experimental value of 6.23 Å.[39] The trilayer (three WS_2 layers) and the surface are shown in Figure 1. The optimized inter-layer distance in the trilayer is 6.13 Å. In the case of the surface, the optimized distance between layers is 6.14 Å, intermediate between those for the trilayer and the bulk (notice that the separation between the two bottom layers in the surface model used here is fixed at 6.15 Å).

We have investigated single-wall WS_2 nanotubes of different chiralities and diameters: arm-chair (8,8), (10,10), (12,12), (14,14), (16,16) nanotubes, and zig-zag (16,0), (20,0), (24,0), (28,0), (32,0) nanotubes. We also studied the representative double-walled (8,8)@(16,16), (10,10)@(16,16), (16,0)@(28,0) and (20,0)@(32,0) nanotubes. Cross section views of these nanotubes are plotted in Figures 1 and 2. The distances between the inner and the outer walls in the double-walled nanotubes are close to 6.21 Å, slightly higher than the interlayer distances for planar systems (6.13-6.15 Å). This trend is consistent with the experimental data on multiwall nanotubes,[40] which also reveals larger interlayer separations than the WS_2 solid.

The cross sections of all the nanotubes are perfectly circular (see Figures 1 and 2). Taking the arm-chair (10,10) and the zig-zag (20,0) nanotubes as specific examples, the maximum (outermost S atoms) and minimum (innermost S atoms) diameters of these nanotubes are 22.4 Å / 16.1 Å in the first tube, and 25.2 Å / 18.8 Å in the second. We then estimated the diameters of the single-wall nanotubes, D_{NT}, by taking the average between the maximum and minimum diameters for each nanotube. This estimation results in diameters of 15.7 Å, 19.2 Å, 22.4 Å, 26.1 Å and 29.4 Å for the arm-chair (8,8), (10,10), (12,12), (14,14) and (16,16) nanotubes, respectively, and 18.4 Å, 22.0 Å, 25.9 Å, 30.2 Å and 34.0 Å for the zig-zag (16,0), (20,0), (24,0), (28,0) and (32,0) nanotubes, respectively.
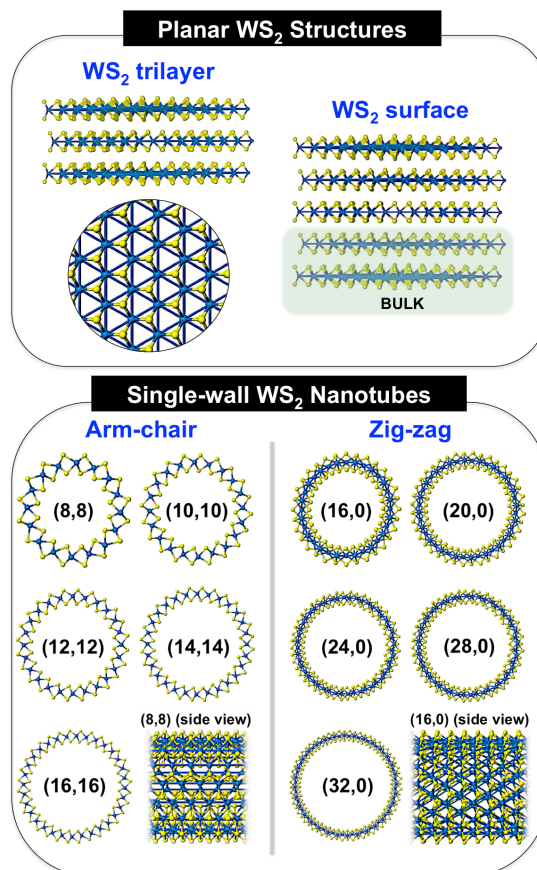

Figure 1. Top panel: optimized structures of the WS_2 trilayer and the surface. Bottom panel: optimized structures of (left) the arm-chair (m,m) single-wall WS_2 nanotubes with m=8, 10, 12, 14, and 16, and (right) the zig-zag (m,0) single-wall WS_2 nanotubes with m=16, 20, 24, 28 and 32. W and S atoms are represented by blue and golden spheres, respectively.

As a test of the robustness and thermal stability of the optimized structures obtained in the calculations, constant temperature molecular-dynamics simulations were performed by heating some nanotubes up to a temperature T = 850 °C, and all the structures were verified to be stable. This result is consistent with the experimental observation that fullerenic-like multilayer WS_2 nanoparticles are thermally stable at this temperature[41].
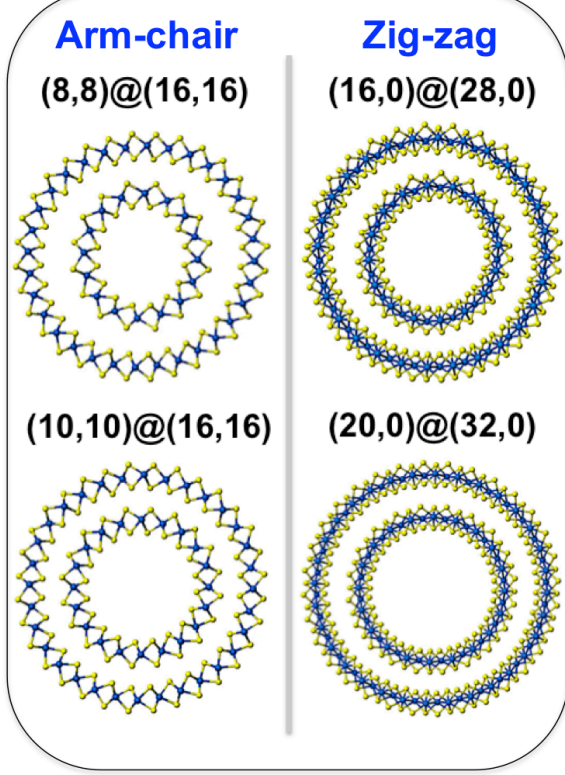
Figure 2. Optimized structures of the: (left) arm-chair (8,8)@(16,16) and (10,10)@(16,16), and (right) (16,0)@(28,0) and (20,0)@(32,0) double-walled WS$_2$ nanotubes. Blue and golden spheres represent W and S atoms, respectively.

4. Adsorption of Molecular Hydrogen

Calculations have been performed to model the adsorption of molecular hydrogen on different layered WS$_2$ structures. As a first step we investigated the adsorption of H$_2$ on the planar WS$_2$ structures: single layer, trilayer and surface. All the non-equivalent possible adsorption sites (on top sites, bridge sites, hollow sites) and orientations of the molecular axis (parallel, perpendicular and tilted with respect to the substrate) were investigated. In the calculations, the positions of the substrate atoms, as well as the interatomic H-H distance were allowed to relax. Results for the most favourable adsorption sites and orientations, those with the highest molecular physisorption energies, are plotted in Figure 3: (a) H$_2$ molecules laying parallel to the layer on top of a W atom; (b) molecules perpendicular to the layer on top of a W atom; (c) molecules parallel to the layer on top of a S atom; (d) molecules perpendicular to the layer on top of a S atom. The calculations reveal that the H$_2$ molecules prefer sitting on top of W atoms, so the coverage will be defined as the fraction of W atoms with an adsorbed H$_2$ molecule. Different coverages, x (monolayer fraction), have been investigated, ranging between low coverage, $x = 0.0625$ ML (one H$_2$ molecule per unit cell of the surface layer), up to full coverage, $x = 1$ ML. Full coverage is achieved with 16 adsorbed molecules per unit cell because the number of W atoms in the unit cell chosen is 16. The adsorption energies per H$_2$ molecule for coverage x are defined by the following expression:

$$E_{ads}(xML) = \frac{[E(pristine) + nE(H_2) - E(xML)]}{n}, \quad (1)$$

where $E(xML)$ is the energy per unit cell of the system with H$_2$ coverage corresponding to a fraction x of a monolayer, E(pristine) is the energy of the corresponding unit cell of the pristine system (no hydrogen adsorbed), and $nE(H_2)$ is the energy of n isolated gas molecules, where n is the number of hydrogen molecules in the unit cell for coverage x. The results for adsorption on a single WS$_2$ layer at the coverage of one H$_2$ molecule per unit cell ($x = 0.0625$ ML) are presented in Table 1.

Table 1. Adsorption energies E_{ads} (in eV) per H$_2$ molecule on a WS$_2$ layer, and distances d_{ads} (in Å) between the H$_2$ molecules and the closest plane of S atoms, for the four relevant adsorption configurations: (a) parallel on top of a W atom, (b) perpendicular on top of W, (c) parallel on top of S, (d) perpendicular on top of S. The coverage is $x = 0.0625$ ML.

Configuration	(a)	(b)	(c)	(d)
E_{ads}(eV)	0.065	0.073	0.048	0.051
d_{ads}(Å)	2.83	2.95	3.41	3.37

The adsorption energies are positive in all cases; that is, molecular adsorption is favourable. Their values are small, typical of the physisorption regime. The calculations reveal two preferential adsorption configurations: these are the configurations (a) and (b), corresponding to adsorption of H$_2$ on top of W atoms, where a triangular hollow formed by three S atoms permits the easy accommodation of physisorbed H$_2$ molecules. The adsorption energies for these two configurations, 0.065 eV and 0.073 eV, respectively, are not too different. The corresponding adsorption distances (distance between the centre of mass of the H$_2$ molecule and the closest plane of S atoms) are 2.83 Å and 2.95 Å for the parallel and perpendicular orientations of the molecule, respectively. This difference is mainly an effect of the orientation: in the perpendicular orientation, the H atom closest to the plane of S atoms is at a distance of 2.57 Å, and this short distance is the reason for the higher physisorption energy of the molecule. The results for adsorption on top of S atoms are also reported in Table 1. The number of S atoms in the upper plane of a WS$_2$ layer is also 16, so the coverage $x = 0.0625$ ML corresponds to the same number of molecules per unit cell as in the case of adsorption on W atoms. Adsorption on S atoms leads to longer adsorption distances compared to adsorption on W atoms, and consequently produces lower adsorption energies. The molecule-layer distances, i.e., the distance between the centre of mass of the H$_2$ molecule and the closest plane of S atoms, are 3.41 Å and 3.37 Å for the (c) and (d) configurations, respectively. These large values also result in a weaker dependence of adsorption energy and adsorption distance on the orientation of the molecule.

Then, the H$_2$ physisorption energies and distances have been monitored as a function of H$_2$ coverage. Four different coverages have been investigated: 0.0625 ML (one H$_2$ molecule per unit cell), 0.25 ML (4 molecules per unit cell), 0.5 ML (8 molecules per unit cell), and 1 ML (16 molecules per unit cell). The results for adsorption on W atoms (configurations called (a) and (b) above) of the single WS$_2$ layer are presented in Table 2. For fixed coverage, the perpendicular configuration yields higher adsorption energies

as compared to the parallel configuration. The adsorption energies per H_2 molecule decrease slightly with increasing adsorption coverage: from 0.065 eV to 0.059 eV for configuration (a), and from 0.073 eV to 0.064 eV for configuration (b). This decrease arises from repulsive interactions between neighbour H_2 molecules: the H_2—H_2 interaction potential is repulsive for distances smaller than 3.4 Å between the two molecules[42]. As a result, adsorption distances increase slightly with coverage for both configurations. The adsorption energies per H_2 molecule and the adsorption distances for the (c) and (d) configurations with the H_2 molecules adsorbed on S atoms (not shown in Table 2) practically do not vary with coverage within the range 0.0625—1 ML, yielding values of 0.048—0.047 eV and 3.36—3.37 Å for configuration (c), and 0.051—0.050 eV and 3.41—3.42 Å, for configuration (d). These values also confirm the idea of a weaker dependence of adsorption energy and adsorption distance on the orientation of the molecule for these two configurations.
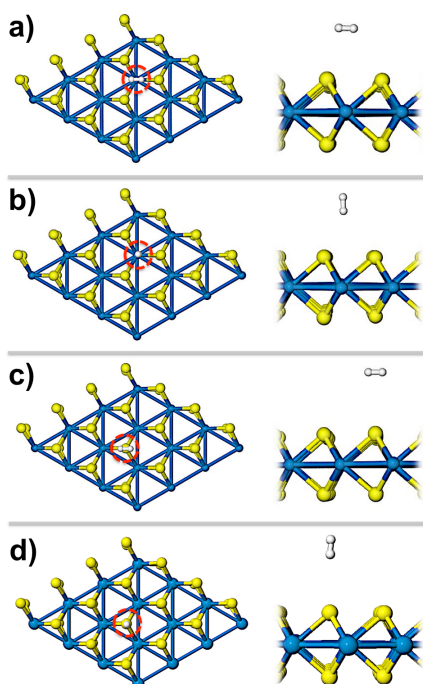

Figure 3. Top (left) and side (right) views of: a) H_2 molecule adsorbed on top of a W atom of a single WS_2 layer with the molecular axis parallel to the layer; b) H_2 molecule adsorbed on top of a W atom with the axis perpendicular to the layer; c) H_2 molecule adsorbed on top of a S atom with the axis parallel to the layer; d) H_2 molecule adsorbed on top of a S atom with the axis perpendicular to the layer. Blue, golden and white spheres represent W, S and H atoms, respectively.

Table 2. Adsorption energies E_{ads} (in eV) per H_2 molecule, and adsorption distances d_{ads} (in Å) between the H_2 molecules and the closest plane of S atoms, for the two most stable adsorption configurations: (a) H_2 on top of a W atom with the axis parallel to the layer; (b) H_2 on top of a W atom with the axis perpendicular to the layer. The results are the same for the WS_2 layer, the trilayer, and the bulk surface.

H_2 Coverage	Config. (a)		Config. (b)	
	E_{ads} (eV)	d_{ads} (Å)	E_{ads} (eV)	d_{ads} (Å)
0.0625 ML	0.065	2.83	0.073	2.95
0.25 ML	0.064	2.84	0.071	2.96
0.5 ML	0.062	2.84	0.067	2.96
1 ML	0.059	2.86	0.064	2.98

It is worth to notice that the numerical results of Table 2 do not change for adsorption on the surface of a trilayer or on the surface of bulk WS_2. This means that the van der Waals interactions between the WS_2 layers do not affect the interaction between H_2 and the outermost layer. However, the H_2 adsorption on the topmost layer of the WS_2 multilayers (trilayer and surface) induces a widening of the distance between the topmost and the second WS_2 layers. This decoupling is enhanced by increasing H_2 coverage: the interlayer distances of 6.13 Å for the pristine trilayer and 6.14 Å for the pristine surface, increase up to 6.21 Å and 6.23 Å, respectively, for full coverage of x = 1 ML. Another relevant observation is that the strength of the adsorption energies is similar to those for H_2 on graphene and other related layered materials.[43-45] A direct comparison with the theoretical work of Petrushenko et al.[45] is possible because these authors used the DFT method with the same exchange–correlation functional and van der Waals formalism as in our present work. They investigated the adsorption of H_2 on graphene, hexagonal BN and a composite of graphene and hexagonal BN. The calculated adsorption energies on the most favourable adsorption sites are 0.069 eV (graphene), 0.067 eV (hBN) and 0.073 eV (composite). These values are quite similar to the optimal adsorption energy of 0.073 on WS_2. Adsorption energies obtained by averaging over the different possible adsorption sites are 0.064 eV (graphene), 0.059 eV (hBN) and 0.067 eV (composite), again close to the average value of 0.059 eV obtained from Table 1. This indicates that the hydrogen storage based on H_2 is similar in these materials.

Similar adsorption behavior occurs in nanotubes. Table 3 gives the results for low coverage of the outermost wall of three double-walled nanotubes, (10,10)@(16,16), (16,0)@(28,0) and (20,0)@(32,0). The coverage is one adsorbed H_2 molecule per nanotube unit cell, comparable to the coverage x = 0.0625 ML in planar layers. The most stable adsorption configurations are again the configurations (a) and (b) described above. The adsorption energies and adsorption distances, which depend on the adsorption configuration but are nearly independent of the nanotube diameter, are very close to those for low coverage, x = 0.0625 ML, on the planar WS_2 structures. We show below that this behaviour is different for chemisorption of atomic hydrogen. When H_2 molecules are adsorbed on the innermost wall of the nanotubes, that is, on the hollow internal surface of the nanotubes, the preferred adsorption configurations are again configurations (a) and (b), and the adsorption energies are practically the same as for adsorption on the external wall. A slight increase in the adsorption distances occurs by increasing the H_2 content. For instance, an increase of 0.03 Å is observed for external adsorption in configuration (a) when the H_2 content increases up to 0.5 ML, and an increase of 0.06 Å for internal adsorption.

Table 3. Adsorption energies E_{ads} per H_2 molecule (in eV), and adsorption distances d_{ads} (in Å) for the most stable adsorption configurations, (a) and (b), on either the outermost or the innermost walls of double wall nanotubes. The results correspond to low coverage: one molecule adsorbed per nanotube unit cell.

Nanotube	Config. (a)		Config. (b)	
	E_{ads} (eV)	d_{ads} (Å)	E_{ads} (eV)	d_{ads} (Å)
(10,10)@(16,16)	0.063	2.83	0.072	2.95
(16,0)@(28,0)	0.061	2.84	0.068	2.96
(20,0)@(32,0)	0.061	2.84	0.068	2.96

An interesting possibility to be explored is the adsorption of more than one hydrogen monolayer on the surface of planar platelets. For this purpose we performed computer simulations in which the starting configuration was formed by H_2 molecules on top of all W and S atoms, which corresponds to 2 ML coverage in the notation used above. All the molecules were initially placed as a single layer parallel to the surface, with their centres of mass separated by a distance of 2.9—3.0 Å from the topmost plane of S atoms, and the molecules were oriented perpendicular to the WS_2 layer. Structural relaxation of the system allowed the hydrogen molecules to optimize their positions, forming two layers as shown in Figure 4. In all cases the molecular axes maintained a nearly perpendicular orientation. The H_2 molecules of the layer closest to WS_2 sit on top of W atoms, like in the case of a single H_2 layer discussed above. These molecules are at a distance of 2.84 Å from the plane of S atoms, very close to the distance of 2.86 Å for 1 ML coverage in Table 2. The H_2 molecules of the upper layer rest on sites above S atoms to optimize their interaction with the WS_2 layer and with the lower H_2 layer. The distance between the two planes formed by the centres of mass of the H_2 molecules in the two layers is 2.52 Å. The average adsorption energy for the two adsorbed layers is 0.058 eV per molecule. This is only a bit smaller than the physisorption energy per molecule (0.064 eV) for one adsorbed H_2 monolayer with the molecules in the perpendicular orientation (see Table 2). In spite of the upper hydrogen layer being more distant from the WS_2 substrate, the similarity of the adsorption energies can be understood as a result of the attractive van der Waals interactions between the two adsorbed hydrogen layers. The calculated energy for desorbing the top H_2 layer is 0.052 eV per molecule, which is not too different from the desorption energy value of 0.064 eV per molecule when only a single layer is adsorbed.
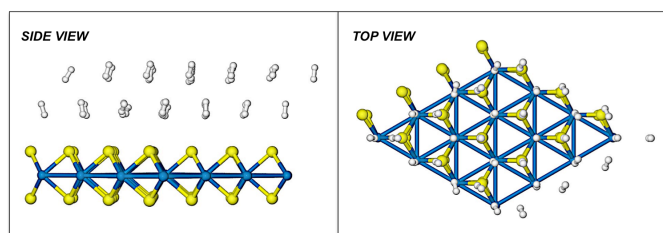

Figure 4. Top and side views of the optimized structure for two full layers of H_2 molecules adsorbed on top of a WS_2 layer. Blue, golden and white spheres represent W, S and H atoms, respectively.

5. Chemisorption of Atomic Hydrogen

The adsorption of a single H atom on the surface of layered WS_2 materials produces a chemisorption state. Figure 5 shows the most stable configuration of H on a single WS_2 layer, chemisorbed on top of an S atom with the S—H bond perpendicular to the layer. The distance between the H and S atoms is 1.43 Å, and the chemisorption energy

$$E_{chem}(H) = E(pristine) + E(H) - E(H@WS_2) \qquad (2)$$

is 1.37 eV. In this equation, E(H) represents the energy of an isolated H atom, and E(H@WS_2) is the energy of the system with the H atom adsorbed. This chemisorption energy really corresponds to coverage x = 0.0625 ML, that is, one H atom per unit cell. By comparison with molecular adsorption discussed above, the bond distance is much shorter, and the bond strength is much higher.

In contrast to the physisorption energies of H_2 on WS_2 nanotubes, which are nearly independent of the nanotube diameter, the chemisorption energies of atomic hydrogen exhibit an interesting correlation with the nanotube diameters. On the nanotubes, the configuration of the chemisorbed H atom is the same as for planar layers. We have calculated the chemisorption energies of H on the outer surface of all the studied single-wall nanotubes for the lowest coverage of 0.0625 ML. The chemisorption energy plotted in Figure 6 has a value of 1.39 eV for the nanotube with the largest diameter, the zig-zag (32,0) nanotube, and then increases linearly as the nanotube diameter decreases, reaching a value of 1.57 eV for the nanotube with the shortest diameter, the arm-chair (8,8) nanotube. No difference is found between the arm-chair and zig-zag nanotubes. This behaviour reflects the enhanced reactivity of the S atoms as the surface curvature increases in the nanotubes. The H chemisorption energy on the (32,0) nanotube is already quite close to the chemisorption energy on the planar layer, 1.37 eV.

Recent experiments of plasma-hydrogenation of WS_2 materials did not reveal the existence of chemisorbed atomic hydrogen.[26] This observation is now supported by the following calculations. The sum of the chemisorption energies of two separated H atoms is approximately 2.7 eV, a value substantially lower than the binding energy between the two H atoms in a free H_2 molecule, 4.52 eV. So, the process of dissociating the H_2 molecule and chemisorbing the two H atoms is energetically very unfavourable. Dissociating the H_2 molecule on the WS_2 surface costs slightly less, but the activation barrier is still high, as discussed next.
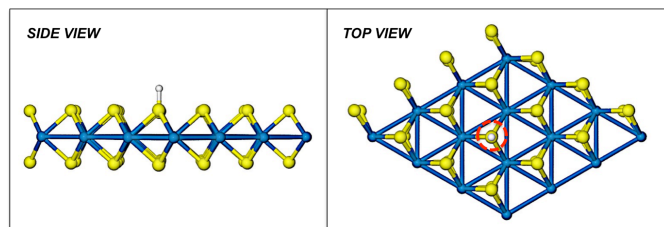
Figure 5. Top and side views of the optimized structure of an H atom chemisorbed on top of an S atom of a single WS$_2$ layer. Blue, golden and white spheres represent W, S and H atoms, respectively.

We have performed CI-NEB calculations to find the minimum energy paths for H$_2$ dissociation on the WS$_2$ single-layer, the bulk surface, and the (20,0)@(32,0) nanotube. This methodology provided results in good agreement with the experiments in other layered materials.[46] The calculated barrier heights for H$_2$ dissociation range between 3.8 eV and 4.0 eV for the different starting (a)—(d) H$_2$ adsorption configurations. Although these barriers are smaller than the dissociation energy of the free H$_2$ molecule, 4.52 eV, the large activation barriers indicate that H$_2$ dissociation leading to atomic H chemisorption is unlikely to take place on the surface of WS$_2$ materials. Of course those barriers are no relevant if chemisorbed H is produced in experiments already starting with atomic hydrogen. In fact, neutral H atoms and H$^+$ cations are generated in a hydrogen plasma, in addition to molecular hydrogen,[10,26] although in a concentration usually too small compared to that of H$_2$.
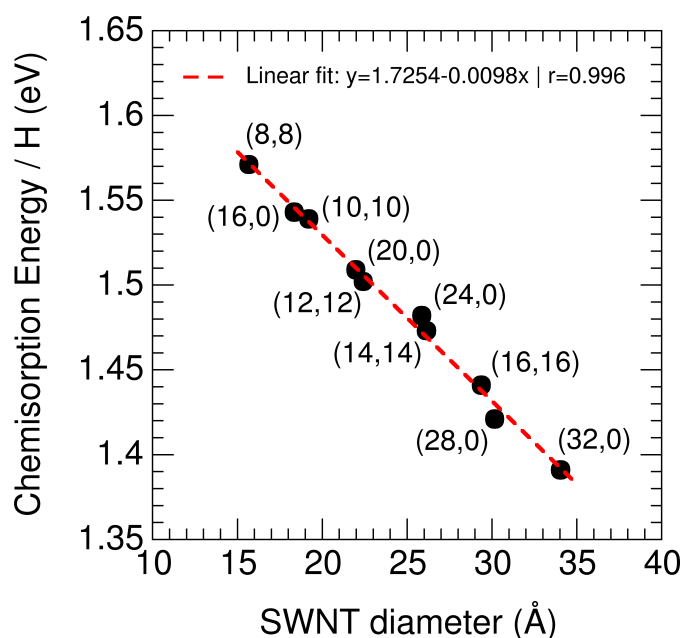
Figure 6. Chemisorption energy per H atom (in eV) as a function of the nanotube diameter (in Å), in the low coverage regime 0.0625 ML, for single-wall nanotubes: arm-chair (8,8), (10,10), (12,12), (14,14), (16,16), and zig-zag (16,0), (20,0), (24,0), (28,0), (32,0) nanotubes. The result of the linear regression is also shown in the figure.

6. Diffusion of H$_2$ and H on the Surface of WS$_2$ Layers

The diffusion of H$_2$ and H on the surface of a WS$_2$ layer has been investigated using the CI-NEB methodology. In the case of H$_2$ the diffusion event analysed is the jump from an initial state with the molecule sitting on its preferred position on top of a W atom to a similar final position on top of a neighbour W atom (see Figure 7). The CI-NEB method generates the path requiring the minimum energy. The calculations were performed for the two relevant initial orientations of the molecular axis, parallel and perpendicular to the WS$_2$ layer, but the orientation can change along the diffusion path. Figure 7 shows the initial and final configurations, as well as the configuration at the stage corresponding to the top of the barrier. The energies along the diffusion path are plotted on the left panels of this figure. The diffusion follows a path along the W—W bond, and the activation barriers are quite low: 0.025 eV in the case of a parallel molecule, and only 0.010 eV for the perpendicular molecule. Consequently, the H$_2$ molecules are expected to be quite mobile on the WS$_2$ surface at room temperature. These low activation barriers are not surprising because the H$_2$ molecule is physisorbed. For comparison, the calculated activation barrier for diffusion of H$_2$ on the surface of graphene is 0.010 eV.[47]
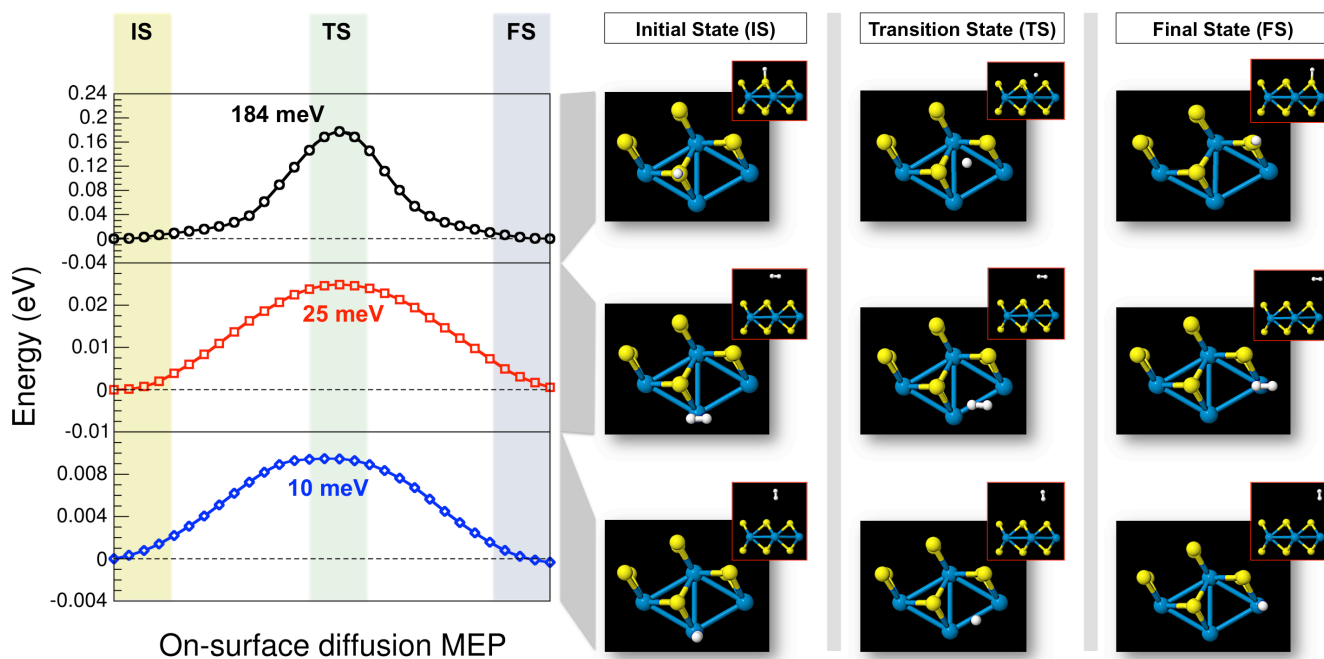
Figure 7. The right panels show top and side views of the initial state, IS, transition state, TS (corresponding to the maximum of the activation barrier), and final state, FS, for the diffusion of H (top panels) and H_2 (middle and bottom panels) on the WS_2 surface. The left panel shows the CI-NEB energy barriers along the minimum energy diffusion paths (MEPs). Blue, golden and white spheres represent W, S and H atoms, respectively.

On the other hand, as shown in Figure 7, the diffusion of an H atom between positions on top of neighbouring S atoms of the surface is quite different. The path is roughly the shortest path between the two S atoms, and the height of the activation barrier is 0.18 eV. Consequently, the mobility of H is much reduced compared to the mobility of H_2. In a previous work by some of us,[10] hydrogenation of hollow WS_2 multiwall nanotubes was performed by exposing the material to a high-pressure (80 kbar) atmosphere of molecular hydrogen at temperatures of 35 ^oC, 200 ^oC and 350 ^oC; that is, near room temperature and above. The pressure-composition-temperature absorption isotherms indicated that the weight percent of absorbed hydrogen is 0.11-0.13%. Since physisorption is generally more efficient at low temperatures, we have performed a set of high pressure hydrogenation experiments in which WS_2 nanoparticles and multiwall nanotubes were kept at temperatures between -196 °C and -50 °C, and several isotherms were measured. The transmission electron microscopy (TEM) analysis revealed concentric semi-spherical WS_2 shells forming giant fullerene-like structures. The nanotubes were 50-150 nm wide and about 20 μm long, and the diameters of the spherical or semi- spherical nanoparticles were in the range of 50-250 nm. As can be observed in Figure 8, the isotherms measured at -196 °C show the increase of hydrogen concentration up to 0.16 wt. % for nanotubes, and up to 0.28 wt. % for nanoparticles. The highest hydrogen concentrations were obtained, however, at -78 °C: 0.29 wt. % for nanotubes and 0.36 wt. % for nanoparticles.

The increase in the hydrogen concentration at low temperatures is substantial, up to three times compared to room temperature. And the fact that hydrogen concentration is higher at -78 °C than at -196 °C is remarkable. Our interpretation is that diffusion, which is generally favoured by higher temperatures, plays a significant role. Diffusion allows the H_2 molecules moving through the material to efficiently reach all the available adsorption sites. The thermal energies, k_BT, at -196 °C and -78 °C are 0.007 eV/molecule and 0.017 eV/molecule, respectively, and the activation barrier for diffusion of H_2 molecules in the perpendicular configuration is 0.010 eV, smaller than k_BT at -78 °C. This rough estimation indicates that diffusion becomes more efficient at T = -78 °C than at -196 °C, explaining the result of larger hydrogen concentration at -78 °C.
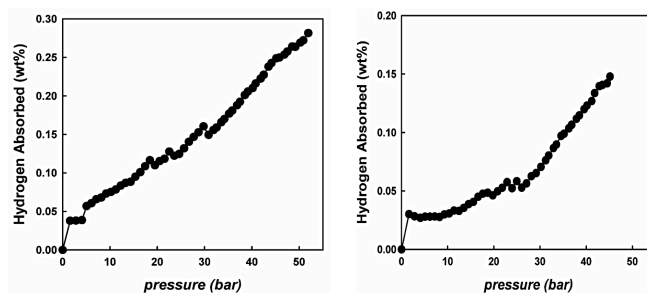

Figure 8. Hydrogen absorption isotherms measured at -196 °C in: (left) giant fullerenic-like WS_2 nanoparticles, and (right) multi-walled WS_2 nanotubes.

Interestingly, the following trend was observed in the high-pressure hydrogenation of multiwall nanotubes measured in the previous work:[10] the amount of hydrogen adsorbed at 200 ^{o}C and 350 ^{o}C is smaller than at 35 ^{o}C. The explanation is that H$_2$ desorption competes with adsorption, and is responsible for the lowering of the amount of adsorbed hydrogen observed at 200 ^{o}C and 350 ^{o}C. Desorption of H$_2$ from the surface of WS$_2$ has an energy cost of 0.06—0.07 eV (see Table 2), and the values of $k_B T$ at 35 ^{o}C, 200 ^{o}C and 350 ^{o}C are 0.027 eV, 0.041 eV and 0.054 eV, respectively; thus, desorption will deplete the amount of adsorbed hydrogen at the two highest temperatures considered. The results for adsorption on nanotubes and nanoparticles at low and high temperatures are shown together in Figure 9. The interesting observation is that a temperature T_m exists that maximizes adsorption. As discussed above, at $T < T_m$ slow diffusion prevents molecular hydrogen from reaching all the available adsorption sites. On the other hand, for $T > T_m$ desorption competes with adsorption.
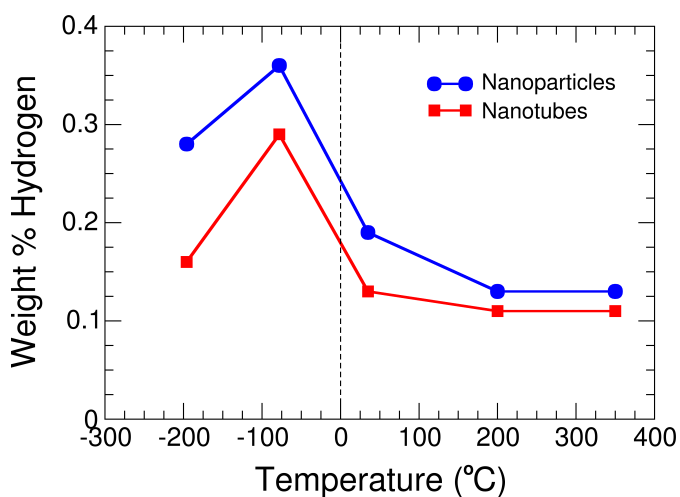
ML. The simulations started by placing the intercalated molecules (one per cell) in an initial position which is below a W atom of the upper WS$_2$ layer and above a S atom of the middle layer, with the molecular axis perpendicular to the layers. This is precisely the configuration called (b) above when viewed with reference to the upper layer of the trilayer. During the structural relaxation, the molecule evolved by moving to a position above a neighbour W atom of the intermediate layer, and changing the orientation of the molecular axis, which ends up oriented parallel to the layers (see Figure 10). At the same time, the separation between the two WS$_2$ layers confining the molecules increased up to 6.21 Å, which is the optimal separation to host the intercalated molecules. The orientation of the molecule is different from its orientation when the molecule is adsorbed on a free WS$_2$ surface, that is, when the molecule is not confined. The reason is that intercalation with the parallel orientation forces a smaller widening of the spatial gap between the two confining layers as compared to the perpendicular orientation.
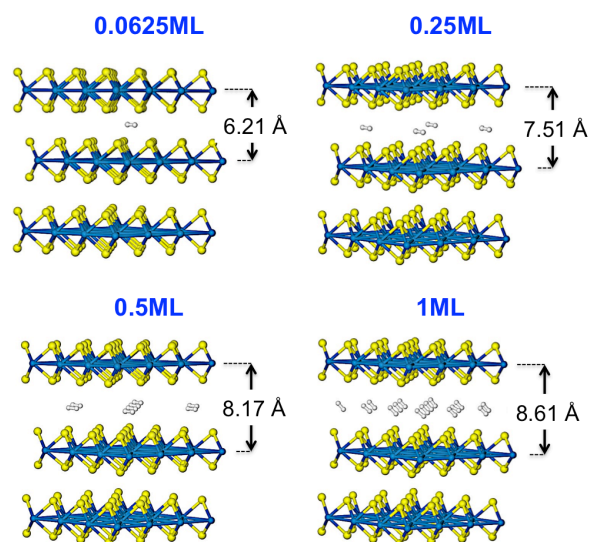

Figure 9. Experimental results for hydrogen adsorption (weight per cent) in multi-walled WS$_2$ nanotubes and giant fullerenic-like WS$_2$ nanoparticles at several temperatures (from Refs. [10, 26], and new results).

Figure 10. Optimal structures for intercalation of molecular hydrogen between the first and the second layers of the WS$_2$ trilayer for different H$_2$ content: 0.0625 ML, 0.25 ML, 0.5 ML and 1ML.

7. Intercalation of Hydrogen in Multilayers and Multiwall Nanotubes

The calculations presented above reveal that H$_2$ can be adsorbed on the surface of WS$_2$ multilayers and nanoparticles, or in the outermost or innermost walls of WS$_2$ nanotubes. To investigate the possibility of intercalation of H$_2$ between WS$_2$ layers we have performed calculations by intercalating the trilayer with increasing amounts of H$_2$. For this purpose, H$_2$ molecules were placed in between the first and the second layers of the trilayer, and the system was allowed to fully relax to reach its lowest energy structure. Four hydrogen concentrations were explored, namely x = 0.0625 ML, 0.25 ML, 0.5 ML and 1ML. As a specific example, we consider the case of the lowest hydrogen concentration, x = 0.0625

Based on this observation, the simulations of the intercalation with higher amounts of hydrogen started with the H$_2$ molecules initially placed on top of W atoms of the middle layer, with the molecular axis parallel to the layers. The main change occurring during structural optimization was the readjustment of the distances between the WS$_2$ layers. Figure 10 shows the final configurations for intercalation with 0.25 ML, 0.5 ML and 1 ML of H$_2$. Table 4 reveals that the distance between the first and the second layer increases substantially as the amount of intercalated hydrogen increases. Another observation is that the final orientation of the intercalated molecules at 1ML of H$_2$ is intermediate between parallel and perpendicular orientations. The expanded separation between the two WS$_2$ layers is responsible for this orientation.

The intercalation energy per hydrogen molecule can be defined by the following expression:

$$E_{int}^{mol}(xML) = \frac{[E(trilayer)+nE(H_2)-E(xML)]}{n}, \qquad (3)$$

where $E(xML)$ is the energy of the unit cell of a trilayer intercalated with a fraction x of a monolayer of H_2, $E(trilayer)$ is the energy of the corresponding unit cell of the pristine trilayer, and $nE(H_2)$ is the energy of n isolated gas molecules, where n corresponds to the number of hydrogen molecules in the unit cell for the intercalate fraction x. The intercalation energy, given in Table 4, is negative in all cases; that is, intercalation is unfavourable. However, a noticeable lowering of the magnitude of the intercalation energy per molecule is observed as x increases, which is due to two factors.

Table 4. Distance between the first and second layers, d_{L1-L2} (in Å), intercalation energy per molecule, E_{int}/H_2 (in eV), layer-layer expansion energy, E_{exp} (in eV), and binding energy per molecule, E_b/H_2 (in eV), for the intercalation of molecular hydrogen between the first and the second layers in the WS_2 trilayer.

	d_{L1-L2} (Å)	E_{int}/H_2 (eV)	E_{exp} (eV)	E_b/H_2 (eV)
0 ML	6.13	-	-	-
0.0625 ML	6.21	-2.34	-1.50	-0.84
0.25 ML	7.51	-1.01	-3.76	-0.07
0.5 ML	8.17	-0.48	-4.42	0.07
1 ML	8.61	-0.19	-4.74	0.11

The first factor can be understood from the column labelled E_{exp} in Table 4. The intercalation of H_2 leads to an increase of the interlayer distance. Then we define the expansion energy as the energy (per unit cell) that would be required to increase the distance between the first and the second layers of a pristine (non-intercalated) trilayer. To be consistent with the sign convention chosen for the adsorption and intercalation energies, we assign the negative sign to the expansion energy cost. The magnitude of the expansion energy becomes larger as the distance between WS_2 layers increases. However E_{exp} varies in a special way. The expansion energy for the increase of the interlayer distance from 6.13 Å to 6.21 Å (distances corresponding to intercalation with 0 ML and 0.0625 ML, respectively) is large. It amounts to -1.50 eV per unit cell, with an expansion energy rate of -1.50/0.07 = -21.4 eV/Å. Next, for the interlayer widening from 6.21 Å to 7.51 Å as a result of increasing the amount of intercalated H_2 from 0.0625 ML to 0.25 ML, the expansion energy rate drops to the value -2.26/1.3 = -1.74 eV/Å. The lowering tendency of the expansion energy rate continues for the interlayer widening from 7.51 Å to 8.17 Å, yielding a value -1.0 eV/Å. In the last step, an expansion energy rate of only -0.72 eV/Å is found for the interlayer widening from 8.17 Å to 8.61 Å. The second factor responsible for the lowering of the magnitude of the intercalation energy per molecule is simply the increasing value of n in the denominator on the right hand side of eq. (3). The difference between the intercalation and expansion energies is the binding energy, E_b, listed in the last column of Table 4. This is negative for low coverage, because the layer-layer expansion is still

small (the distance between the W planes of the two adjacent layers is 6.21 Å) and the intercalated molecules sample the repulsive part of the molecule-WS_2 potential. Then, as the amount of intercalated H_2 increases, the binding energy turns positive since the large interlayer expansion allows the H_2 molecules sampling the attractive part of the molecule-WS_2 potential. At this limit, higher binding energies are obtained compared to adsorption on a free WS_2 surface due to the interaction of the molecule with the two confining layers.

It can be noticed from previous sections that the distance between chemisorbed H atoms and the surface of a WS_2 layer (1.43 Å) is about one half of the distance between physisorbed H_2 molecules and the surface of WS_2 (2.83-2.98 Å). Consequently, one might suggest that dissociation of the intercalated H_2 molecules could be favourable because the interlayer expansion will be less for intercalated atomic hydrogen. For our purposes the most convenient definition of the intercalation energy of H atoms is the following:

$$E_{int}^{at}(xML) = \frac{[E(trilayer)+nE(H)-E(xML)]}{n}. \qquad (4)$$

In this equation, $E(trilayer)$ is the energy of the unit cell of a pristine WS_2 trilayer, $E(xML)$ is the energy of the unit cell of the trilayer intercalated with a fraction x of a monolayer of H atoms, $E(H)$ is the energy of a free H atom, and n is the number of hydrogen atoms in the unit cell for the intercalate fraction x. In contrast to intercalation of molecular hydrogen, intercalation of atomic hydrogen gives positive intercalation energies (see Table 5); that is, the intercalated systems are energetically stable with respect to the clean trilayer and free H atoms.

Table 5. Distance between the first and second layers, d_{L1-L2} (in Å), and intercalation energy per atom, E_{int}/H (in eV), for the intercalation of atomic hydrogen between the first and second layers in the WS_2 trilayer. Results are given for increasing H content.

Coverage	d_{L1-L2} (Å)	E_{int}/H (eV)
0 ML	6.14	-
0.25 ML	6.15	1.15
0.5 ML	6.17	1.32
0.75 ML	6.21	1.36
1 ML	6.25	1.38

The intercalated H atoms become attached to S atoms, reproducing the behaviour already seen in Figure 5. All the H atoms in Figure 11 are attached to S atoms of the upper basal plane of the middle WS_2 layer, but binding energies and distances do not change when part of the H atoms are attached to S atoms of the upper WS_2 layer. Intercalation increases slightly the distance between adjacent WS_2 layers, and this effect is enhanced by increasing the amount of intercalated H. However, by comparing Tables 4 and 5, it is worth noticing that the forced separation between WS_2 layers induced by

intercalation of atomic hydrogen is quite small in comparison to intercalation of H_2. The reason for this is that the H atom is small and its binding to S is strong, so it can be easily accommodated between the adjacent WS_2 layers. This also justifies that the intercalation energies per atom in Table 5 are close to the chemisorption energies (1.37 eV) of H atoms on the surface of a single WS_2 layer. However, the experimental Raman measurements did not detect H—S bonds (see below).[26] We conclude that the amount of atomic hydrogen on the surface or intercalated between layers of WS_2 materials is non-significant because H_2 has a high dissociation energy, and perhaps there was not enough atomic H in the RF plasma.
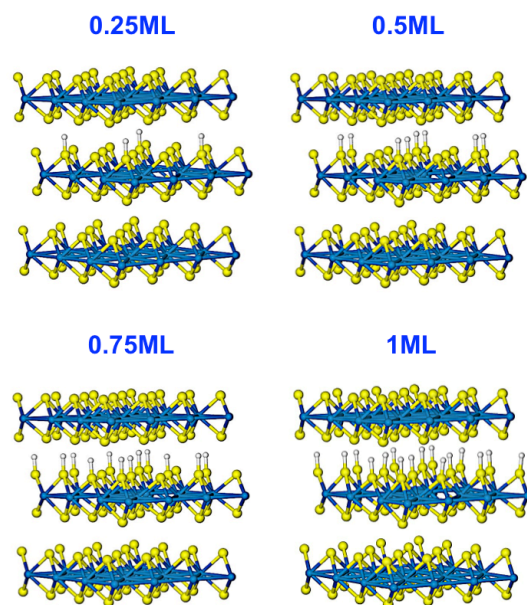

Figure 11. Optimal structures for the intercalation of atomic hydrogen between the first and the second layers of the WS_2 trilayer for different H content (0.25 ML, 0.5 ML, 0.75 ML and 1ML). The H atoms are attached to S atoms belonging to the upper basal plane of the second WS_2 layer. Blue, golden and white spheres represent W, S and H atoms, respectively.

The intercalation energies in Table 5 are positive. This is because the reference in eq. (4) is formed by the free H atoms. To compare these intercalation energies with the intercalation energies of H_2 molecules given in Table 4, both should be measured with respect to the same reference and this is the system of free molecules. First, the number of H atoms intercalated in the cell should be the same in the two cases, so if the coverage of molecular hydrogen is x, the comparable coverage of atomic hydrogen should be 2x. In this way we can compare the configurations of 4 molecules per cell ($x(H_2) = 0.25$ ML) and 8 atoms per cell ($x(H) = 0.5$ ML), and also the configurations of 8 molecules per cell ($x(H_2) = 0.50$ ML) and 16 atoms per cell ($x(H) = 1$ ML). On the other hand, the dissociation energy of the H_2 molecule into two H atoms has to be added (with negative sign) to the atomic intercalation energies. In this way, the energy to intercalate 4 molecules in the cell is (-1.01 eV)×4 = -4.04

eV, or -1.01 eV per molecule, and the energy to dissociate 4 free molecules and intercalate those 8 atoms in the cell is (-4.52 eV)×4 + (1.32 eV)×8 = -7.75 eV, or -1.88 eV per molecule. A similar calculation gives -0.48 eV/molecule for the energy necessary to intercalate 8 molecules in the cell, and -0.88 eV/molecule for the energy to dissociate 8 molecules and intercalate the 16 atoms in the cell (notice that a negative sign indicates an endothermic process). In conclusion, atomic intercalation is unfavourable with respect to molecular intercalation if one accounts for the energy required to dissociate the H_2 molecules.
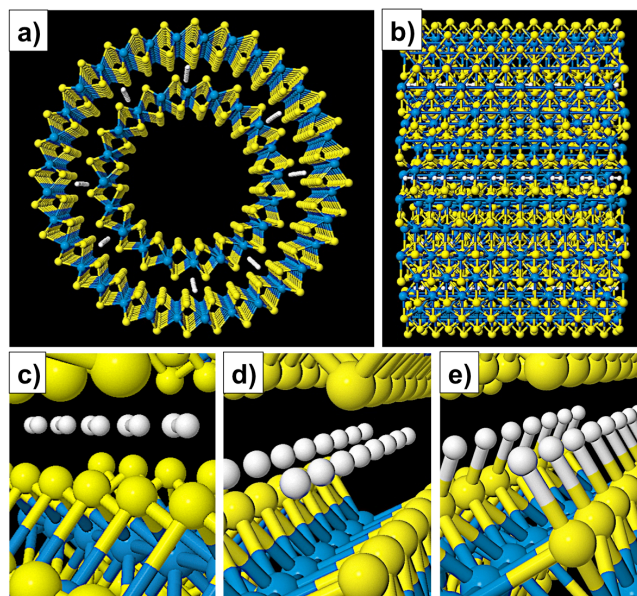

Figure 12. Initial state in three different views, panels (a), (b) and (c), and final state, panel (e), for H_2 molecules intercalated between the walls of a (10,10)@(16,16) nanotube. Eight rows of H_2 molecules have been intercalated, and for the nanotube fragment shown each row contains eight molecules. Panels (c), (d) and (e) show three representative steps along the spontaneous H_2 dissociation. In the (c), (d) and (e) panels, the upper and bottom WS_2 layers correspond to the outer and inner nanotubes, respectively.

An interesting new effect occurs when H_2 is intercalated in multiwall WS_2 nanotubes. The conclusions arise from simulations of the intercalation of H_2 into the double wall nanotubes (10,10)@(16,16) and (20,0)@(32,0). The increased separation between the two walls of the nanotube induced by intercalation of H_2 would result in a change of the radii of the concentric tubes, at least an increase of the radius of the external tube, and perhaps also a decrease of the radius in the inner tube. Those radii changes modify the interatomic distances in each tube, and produce substantial elastic stresses. The energy cost of such processes is much larger than the energy cost to separate two planar WS_2 layers. Another possibility would be a drastic local change of the structure of the tubes around the intercalated molecules, but this is also energetically costly and quite unfavourable. The alternative

and more efficient route chosen by the system, and observed in the simulations, is that the intercalated H_2 molecules spontaneously dissociate and the H atoms form bonds with S atoms, preferentially with S atoms of the inner tube, as shown in Figure 12. Eight rows of molecules have been intercalated, each row parallel to the axis of the nanotube, and the positions of the rows have been chosen in such a way as to maintain substantial distances between adjacent rows. Different views of the starting configuration are shown in panels a), b) and c) of Figure 12. Panel e) shows the final configuration, with the hydrogen molecules dissociated and the H atoms bonded to S atoms, and panel d) represents an intermediate state in the scission path. The radii of the two concentric nanotubes did not change in the dissociation process. The behaviour of H_2 intercalated in multiwall nanotubes is qualitatively different from that observed for intercalation on planar multilayers. The difference arises from the geometry of the multiwall nanotubes, in which an expansion of the tube-tube distance produces an internal distortion of the rigid structure on each nanotube. In comparison, the expansion of the interlayer distance in planar multilayers is easier because the interlayer expansion does not affect the rigid internal structure of the layers. This argument, which explains the results of the simulations, is based on the assumption that the concentration of H_2 molecules intercalated between planar WS_2 layers is enough to produce the expansion of the interlayer distance. It is clear that this is the case for the concentrations investigated in this work, in particular for the lowest one, x = 0.0625 ML. However, this behaviour can change for diluted H_2 concentrations. As an extrapolation we predict that dissociation of H_2 intercalated between planar WS_2 multilayers will occur for very low concentration of H_2, much lower than those investigated here. Verifying this prediction is computationally hard because it needs enlarging the unit cell to sizes much larger than the sizes considered here.

To complete the previous analysis we have studied the diffusion mechanism of an H atom intercalated in a (10,10)@(16,16) nanotube. In the starting configuration, the H atom is chemisorbed on an S atom of the inner (10,10) nanotube (low coverage regime of 0.0625 ML). Using the CI-NEB method two different minimum energy paths (MEP) have been investigated. Path (a) corresponds to the unconstrained MEP from the initial configuration towards a final one with the H atom chemisorbed on the closest S atom of the inner nanotube. Path (b) is a constrained MEP with the same initial and final states as in (a) but this time imposing an intermediate step with the H atom chemisorbed on the closest S atom of the outer (16,16) nanotube. The activation energy barrier for path (a) is 0.23 eV. For path (b), we have found a first barrier of 0.32 eV separating the initial chemisorbed state from the intermediate (constrained) state, and a second barrier of nearly identical height separating the intermediate state from the final chemisorbed state. Consequently, route (a) is more favourable. The diffusion barriers of H atoms intercalated into the MEPs are a bit higher than in the case of diffusion on the surface of a planar layer (0.18 eV). We interpret this feature as an effect of confinement, which hinders the activation of the normal modes associated with the S—H stretching allowing the detachment of the chemisorbed H atom, and makes

diffusion more difficult. This is why diffusion of atomic hydrogen, either on the surface or intercalated into layers of WS_2, will be difficult at room temperature.

Earlier in this Section (see Table 4) it was noticed that intercalation of 0.0625 ML of H_2 in a WS_2 trilayer expands the interlayer distance from 6.13 Å to a value of 6.21 Å, with an associated energy cost required for this expansion. A remarkable observation from Section 4 is that adsorption of a full H_2 monolayer on top of a WS_2 trilayer induces an increase in the distance between the topmost and the second WS_2 layers, from 6.13 Å to 6.21 Å (or from 6.14 Å to 6.23 Å in the case of the WS_2 bulk surface). The consequence is that intercalating 0.0625 ML of H_2 in a trilayer with its surface fully covered by H_2 will not pay the penalty of the expansion energy. This opens a new door to the intercalation process worth to be explored in the future. That is, the presence of adsorbates on the top layer may facilitate the intercalation of species between the layers. A related issue is the dynamical mechanism for the intercalation. Direct insertion of H_2 (or H) from the surface following a path crossing the first WS_2 layer to reach intercalation positions between layers is expected to encounter high barriers. A more appropriate mechanism would be the entrance between layers at the lateral edges of the material.

8. Theoretical Raman Spectroscopy

In a previous work we reported a series of experimental micro-Raman spectra of WS_2 nanoparticles (NPs): a) non-hydrogenated NPs, b) RF plasma hydrogenated NPs, and c) RF plasma hydrogenated NPs vacuum annealed up to 450 °C.[26] The three spectra correspond to the black-solid lines in Figure 13. The aim of these experiments was to confirm that H_2 molecules had been adsorbed on the NPs. A prominent peak centred at ~4150 cm^{-1} was observed for the hydrogenated samples only, and was attributed to the H—H stretching mode in H_2 molecules.[48-50] This was confirmed by heating the hydrogenated samples in vacuum up to 450 °C. The intensity of the H_2 peak gradually decreased until vanishing after annealing (see Figure 13).
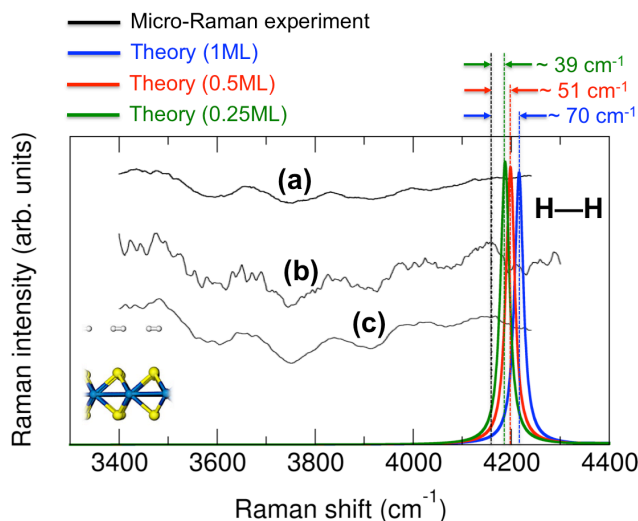
Figure 13. Black-solid lines are measured micro-Raman spectra of WS$_2$ nanoparticles: (a) non-hydrogenated, (b) plasma hydrogenated, (c) plasma hydrogenated and vacuum annealed up to 450 °C. A vertical black-dashed line indicates the location of the experimental H$_2$ peak at 4150 cm^{-1}. The blue, red and green-solid lines are the calculated non-resonant Raman peaks of H$_2$ molecules physisorbed on a planar WS$_2$ layer for coverages of 1 ML, 0.5 ML and 0.25 ML, respectively. Mismatch between theory and experiment is indicated in the three cases.

Motivated by those experiments, and in order to reinforce the validity of our structural hydrogenation model, we have calculated the non-resonant Raman spectra for the optimized physisorption configurations corresponding to three H$_2$ coverages on a single planar WS$_2$ layer. The coverages are 1 ML, 0.5 ML and 0.25 ML. For this purpose we have used an approach based on second order response. Specifically, the second order derivative of the electronic density matrix with respect to a uniform electric field has to be computed. This is done within the context of DFT[51] implemented in the QUANTUM ESPRESSO code.[28] In non-resonant Stokes Raman spectra of harmonic solids and surfaces, the peak intensities can be obtained within the Placzek approximation.[52] This procedure yields the effective charges and dielectric tensor, the Raman tensor and the dynamical matrix, which finally permits the calculation of the Raman cross sections by applying Acoustic Sum Rules. In the calculations we force both translational and rotational modes to zero frequency. This approach proved to yield results in excellent agreement with experiment.[53]

In Figure 13 the calculated non-resonant Raman spectrum of adsorbed H$_2$ exhibits a pronounced peak whose position depends on the adsorption coverage. For 1 ML, 0.5 ML, and 0.25 ML coverages the peaks are centred at 4216 cm^{-1}, 4197 cm^{-1} and 4185 cm^{-1}, respectively. The agreement with the experimental peak at 4150 cm^{-1} is excellent and confirms that the peak is associated to the stretching mode of the physisorbed molecules. The mismatch, smaller in all cases than 70 cm^{-1}, can be due to two factors. The first one concerns the approximations introduced by the theoretical method. The second is the deviation in the real samples from the

specific H$_2$ coverages assumed in the calculations. In fact, Figure 13 shows that lowering the content of adsorbed H$_2$ induces a slight shift in the spectrum, because the interaction between neighbour molecules indeed affects the stretching of the individual molecules. On the other hand, the fact that the substrate in the Raman calculations is a planar WS$_2$ layer is not expected to introduce errors because the nanoparticles in the experiment are quite large.

9. Summary and Conclusions

The interaction of hydrogen with planar WS$_2$ multilayers and single and double-wall nanotubes has been investigated using the density functional formalism with van der Waals corrections. H$_2$ molecules deposited on the surfaces of WS$_2$ multilayers and nanotubes are physisorbed preferentially on top of the W atoms, and the adsorption energies (0.06—0.07 eV/molecule) and distances depend weakly on the coverage. For coverages in excess of one monolayer, a second layer is formed with the H$_2$ molecules on top of S atoms. In contrast, atomic hydrogen forms chemisorption bonds (of strength 1.4—1.6 eV/atom) with the external S atoms. In the case of nanotubes there is an inverse correlation between the bond strength and the nanotube diameter because a decrease in the diameter enhances the curvature and then the chemical reactivity of the nanotubes. While the chemisorption state is favourable starting with free H atoms, the chemisorption energy of two H atoms does not compensate for the energy required to dissociate the H$_2$ molecule.

Diffusion of the H$_2$ molecule on the surface of WS$_2$ from one W atom to a neighbour W atom is easy, with small activation barriers between 0.010 eV and 0.025 eV, depending on the initial orientation of the molecular axis. The magnitude of these barriers serves to rationalize previous and new experimental results for the observed dependence of hydrogen concentration with temperature. The activation barriers for the diffusion of individual H atoms are one order of magnitude larger. Intercalating H$_2$ molecules between adjacent planar WS$_2$ layers is an endothermic process, although the main energy cost occurs for low H$_2$ concentration, and the intercalation energy per H$_2$ molecule decreases as the concentration of intercalated molecules increases. Intercalation of free H atoms is energetically favourable, but again the intercalation energy does not compensate for the cost of dissociating the molecules. This theoretical observation of energetically favourable intercalation of atomic H will allow improving the outcome of hydrogen adsorption experiments. The concentration of atomic hydrogen in the RF plasma used in our previous studies was about 1.5 % and, therefore, resulted in low atomic H intercalation. We believe that using higher atomic H concentration in the plasma will improve H intercalation towards highly desired applications for renewable energy storage systems.

An interesting effect occurs when H$_2$ molecules are intercalated between the two walls of a double wall nanotube. In this case, the rigidity of the structure induces the dissociation of the confined molecules. Diffusion of individual intercalated atoms encounters barriers with a height similar to that for diffusion on an open surface. A remarkable result is that the presence of a full H$_2$ monolayer adsorbed on top of the first WS$_2$ layer of a multilayer strongly facilitates the intercalation of H$_2$ between WS$_2$ layers

underneath. This opens up a new door to intercalation processes. Finally, the calculated Raman peak corresponding to the H-H stretching mode of H_2 molecules adsorbed on a planar WS_2 surface is in very good agreement with experiment.

Overall, the calculations presented here have clarified the different processes and mechanisms related to the interaction of hydrogen with WS_2 nanomaterials. In this way we provide a solid basis for the interpretation and further improvement of the experiments on adsorption and storage of hydrogen on these layered materials.

Acknowledgements

Notes and References

1. A. Gupta, T. Sakthivel, S. Seal, *Prog. Mater. Sci.* **73**, 44-126 (2015).

2. F. Mak, C. Lee, J. Hone, J. Shan, T. F. Heinz, *Phys. Rev. Lett.* **105**, 136805 (2010).

3. A. Splendiani, L. Sun, Y. Zhang, T. Li, J. Kim, C.-Y. Chim, G. Galli, F. Wang, *Nano Lett.* **10**, 1271-1275 (2010).

4. M. Pumera, A. Huiling Loo, *TrAC-Trend. Anal. Chem.* **61**, 49-53 (2014).

5. Q. H. Wang, K. Kalantar-Zadeh, A. Kis, J. N. Coleman, M. S. Strano, *Nature Nanotech.* **7**, 699-712 (2012).

6. D. Jariwala, V. K. Sangwan, L. L. Lauhon, T. J. Marks, M. C. Hersam, *ACS Nano* **8**, 1102-1120 (2014).

7. M. Chhowalla, H. S. Shin, G. Eda, L. J. Li, K. P. Loh, H. Zhang, *Nature Chem.* **5**, 263-275 (2013).

8. X. Duan, J. Xu, Z. Wei, J. Ma, S. Gou, H. Liu, S. Dou, *Small Methods* **1**, 1700156 (2017).

9. Y. Zhang, Q. Zhou, J. Zhu, Q. Yan, S. X. Dou, W. Sun, *Adv. Funct. Mater.* **27**, 1702317 (2017).

10. A. Laikhtman, Sh. Michaelson, A. Hoffman, T. K. Kim, H. R. Moon, A. Zak, *Int. J. Hydrogen Energy* **39**, 9837-9841 (2014).

11. K. Huang, Y. Liu, J. Zhang, J. Cao, Y. Liu, *Biosens. Bioelectronics* **67**, 184-191 (2015).

12. K. Huang, Y. Liu, J. Zhang, Y. Liu, *Sensors and Actuators B-Chem.* **209**, 570-578 (2015).

13. Y. Yuan, R. Li, Z. Liu, *Anal. Chem.* **86**, 3610-3615 (2014).

14. X. Yin, J. Cai, H. Feng, Z. Wu, J. Zou, Q. Cai, *New J. Chem.* **39**, 1892-1898 (2015).

15. J. Huang, L. Ye, X. Gao, H. Li, J. Xu, Z. Li, *J. Mater. Chem. B* **3**, 8180-8187 (2015).

16. I. Cabria, M. J. López, J. A. Alonso, *Handbook on Nanophysics*, ed. K. Sattler, Vol. **5**, 41.1-41.16. CRC Press (2011).

17. J. A. Alonso, I. Cabria, M. J. López, *J. Mater. Res.* **28**, 589-604 (2013).

18. M. J. López, I. Cabria, J. A. Alonso, *J. Chem. Phys.* **135**, 104706 (2011).

19. P. Merino, M. Švec, J. I. Martínez, P. Mutombo, C. González, J. A. Martín-Gago, P. L. de Andrés, P. Jelínek, *Langmuir* **31**, 233-239 (2015).

20. H. González-Herrero, J. M. Gómez-Rodríguez, P. Mallet, M. Moaied, J. J. Palacios, C. Salgado, M. M. Ugeda, J-Y. Veuillen, F. Yndurain, I. Brihuega, *Science* **352**, 437-441 (2016).

21. J. O. Sofo, A. S. Chaudhari, G. D. Barber, *Phys. Rev. B* **75**, 153401 (2007).

22. L. Hao, Y. Liu, Y. Du, Z. Chen, Z. Han, Z. Xu, J. Zhu, *Nanoscale Res. Lett.* **12**, 567 (2017).

23. J. Chen, F. Wu, *Appl. Phys. A* **78**, 989-994 (2004).

24. J. Chen, S. L. Li, Z. L. Tao, *J. Alloys Compounds*, **356–357**, 413-417 (2003).

25. R. Tenne, L. Margulis, M. Genut, G. Hodes, *Nature* **360**, 444-446 (1992).

26. A. Laikhtman, G. Makrinich, M. Sezen, M. M. Yildizhan, J. I. Martinez, D. Dinescu, M. Prodana, M. Enachescu, J. A. Alonso, A. Zak, *J. Phys. Chem. C* **121**, 11747-11756 (2017).

27. N. Song, Y. Wang, S. Ding, Y. Yang, J. Zhang, B. Xu, L. Yi, Y. Jia, *Vacuum* **117**, 63-67 (2015).

28. S. Baroni, A. D. Corso, S. Gironcoli, P. Giannozzi, *QUANTUM ESPRESSO Package* **2005**, in www.quantum-espresso.org

29. G. Kresse, D. Joubert, *Phys. Rev. B* **59**, 1758-1775 (1999).

30. J. P. Perdew, K. Burke, M. Ernzerhof, *Phys. Rev. Lett.* **77**, 3865-3868 (1996).

31. S. Grimme, *J. Comput. Chem.* **27**, 1787-1799 (2006).

32. M. Elstner, P. Hobza, T. Frauenheim, S. Suhai, E. Kaxiras, *J. Chem. Phys.* **114**, 5149-5155 (2001).

33. J. D. Dunitz, A. Gavezzotti, *Acc. Chem. Res.* **32**, 677-684 (1999).

34. M. Methfessel, A. T. Paxton, *Phys. Rev. B* **40**, 3616-3621 (1989).

35. H. J. Monkhorst, J. D. Pack, *Phys. Rev. B* **13**, 5188-5192 (1976).

36. *Classical and Quantum Dynamics in Condensed Phase Simulations*, Editors B. J. Berne, G. Cicotti, D. F. Coker. World Scientific Publishing Company: Singapore (1988).

37. G. Henkelman, H. Jonsson, *J. Chem. Phys.* **113**, 9978-9985 (2000).

38. G. Henkelman, B. P. Uberuaga, H. Jonsson, *J. Chem. Phys.* **113**, 9901-9904 (2000).

39. J. A. Wilson, A. D. Yoffe, *Adv. Phys.* **18**, 193-335 (1969).

40. A. Zak, L. Sallacan-Ecker, A. Margolin, M. Genut, R. Tenne, *Nano* **4**, 91-98 (2009).

41. Ch. Schuffenhauer, G. Wildermuth, J. Felsche, R. Tenne, *Phys. Chem. Chem. Phys.* **6**, 3991-4002 (2004).

42. Y. Okamoto, Y. Miyamoto, *J. Phys. Chem. B* **105**, 3470-3474 (2001).

43. I. Cabria, M. J. López, J. A. Alonso, *Carbon* **45**, 2649-2658 (2007).

44. I. Cabria, M. J. López, J. A. Alonso, *Phys. Rev. B* **78**, 075415 (2008).

45. I. K. Petrushenko, K. B. Petrushenko, *Int. J. Hydrogen Energy* **43**, 801-808 (2018).

46. J. I. Martínez, J. I. Martín-Gago, J. Cernicharo, P. L. de Andrés, *J. Phys. Chem. C* **118**, 26882-26886 (2014).

47. F. Costanzo, P. L. Silvestrelli, F. Ancilotto, *J. Chem. Theory Comput.* **8**, 1288-1294 (2012).

48. B. Panella, M. Hirscher, *Phys. Chem. Chem. Phys.* **10**, 2910-2917 (2008).

49. C. M. Hartwig, J. Vitko, *Phys. Rev. B* **18**, 3006-3014 (1978).

50. B. C. Schmidt, F. M. Holtz, J. M. Bény, *J. Non-Cryst. Solids* **240**, 91-103 (1998).

51. M. Lazzeri, F. Mauri, *Phys. Rev. Lett.* **90**, *036401* (2003).

52. P. Brüesch, *Phonons: Theory and Experiments II* (Springer, Berlin, 1986).

53. J. Azpeitia, G. Otero-Irurueta, I. Palacio, J. I. Martínez, N. Ruiz del Árbol, G. Santoro, A. Gutiérrez, L. Aballe, M. Foerster, M. Kalbac, V. Vales, F. J. Mompeán, M. García-Hernández, J. A. Martín-Gago, C. Munuera, M. F. López, *Carbon* **119**, 535-543 (2017).
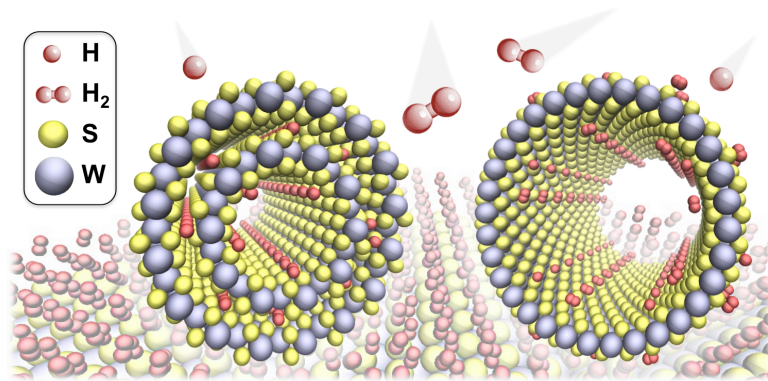
TOC. First-principles calculations, supported by new experimental evidences, have been used to clarify the different processes and mechanisms related to the interaction of hydrogen with WS$_2$ nanomaterials.